Main-chain swollen liquid crystal elastomers: A molecular simulation study

Gregor Skačej[*a,c] **and Claudio Zannoni**[b]

We have performed large-scale off-lattice computer simulations in a model system of swollen main-chain liquid-crystalline elastomers, constituted of weakly reticulated soft Gay-Berne chains, investigating both nematic and smectic morphologies. We present isostress Monte Carlo results for temperature-scan and stress-strain experiments, and connect to typical experimental observables, such as sample dimensions, specific heat, deuterium magnetic resonance spectra, and scattered X-ray patterns. We find that the results reproduce the main features of main-chain elastomers, e.g., a pronounced strain-alignment coupling and the existence of two (nematic-isotropic and smectic-nematic) order-disorder phase transitions. The nematic-isotropic transition in our system turns out to be weakly first-order.

1 Introduction

Liquid crystal elastomers (LCEs) — polymer networks with embedded mesogenic units — are soft functional materials that respond to external stimuli (such as temperature variation, external field, or ultraviolet light) with macroscopic elastic deformations[1,2]. Although qualitatively the behaviour of these systems is reasonably understood, their application for actual sensing devices or actuators[3] requires a more profound insight at the microscopic level. This insight can be gained in principle from molecular simulations; however, not much work has been done in this direction until now. In part, this is because it is not easy to define a microscopic model that is able to capture the basic mesogenic nature of the system and that can be simulated notwithstanding the difficulties of equilibrating three-dimensional networks. (These difficulties arise from chain entanglement and topological constraints due to the linkers.) The early simulation attempts were mostly based on a lattice description of LCEs, which, however, turned out to have only limited predictive power, especially as far as the strain-alignment coupling is concerned[4–7]. Moreover, lattice modeling cannot handle the interesting case of smectic elastomers[8,9], due to the inherent absence of translational degrees of freedom. On the other hand, the existing off-lattice simulation studies were mainly devoted to liquid crystal polymers in the bulk[10,11], or nanoconfined[12], with only preliminary work performed on crosslinked LCE and on the simulation of stress-strain or actuation-related experiments[13].

Therefore, in the present study we readdress the issue, starting from a full molecular description of crosslinked polymeric chains with linked anisotropic mesogenic units as building blocks, and carrying out large-scale Monte Carlo (MC) simulations in this model system. We focus on main-chain systems, significantly swollen with a liquid-crystalline solvent, which are characterised by a greater mobility of polymeric chains, while also being similar (in various aspects) to samples used in experiments by Urayama et al.[14,15]. This work aims at reproducing some of the basic experiments involving the nematic-isotropic order-disorder transition: temperature scans and stress-strain runs, with the stress applied along the director in the ordered nematic phase. More in detail, the simulation output is used to predict selected experimental observables such as sample dimensions, specific heat, deuterium magnetic resonance spectra, and scattered X-ray patterns.

2 Model: Intermolecular interactions

To model the interactions between mesogenic units, we used the soft-core Gay-Berne potential[16]. The original Gay-Berne (GB) potential[17] is an anisotropic Lennard-Jones-like potential that turned out to be quite successful in simulating liquid crystalline phases: isotropic, nematic, and smectic[18]. The recent soft-core modification[16] consists of reducing the steepness of the repulsive part of the GB potential, replacing the standard 12 inverse power dependence on interparticle separation with a linear one. The possibility of limited particle-particle "interpenetration" that the potential allows, offers a

ᵃ Faculty of Mathematics and Physics, University of Ljubljana, Jadranska 19, SI-1000 Ljubljana, Slovenia. E-mail: gregor.skacej@fmf.uni-lj.si
ᵇ Dipartimento di Chimica Fisica ed Inorganica and INSTM - CRIMSON, Università di Bologna, Viale Risorgimento 4, I-40136 Bologna, Italy. E-mail: claudio.zannoni@unibo.it
ᶜ NAMASTE Center of Excellence, Jamova 39, SI-1000 Ljubljana, Slovenia.

simplified description of a flexible molecular system, where two interacting particles yield to some extent rather than just harshly repelling each other. In addition, it facilitates MC equilibration, without significantly affecting the phase behaviour of the molecular system as a whole. In order to be more precise on the form of the model potential we employed in this work, let us consider a pair of uniaxial molecules, i and j, with the orientations of their long axes given by the unit vectors $\mathbf{u}_i$ and $\mathbf{u}_j$, respectively, and their centres separated by the intermolecular vector $\mathbf{r}_{ij}$. Moreover, let $r_{ij} = |\mathbf{r}_{ij}|$ and $\hat{\mathbf{r}}_{ij} = \mathbf{r}_{ij}/r_{ij}$. Then the original GB interaction energy for the molecular pair is given by[17]

$$U_{ij}^{GB} = 4\varepsilon_{ij}\left\{\left[\frac{\sigma_s}{r_{ij} - \sigma_{ij} + \sigma_s}\right]^{12} - \left[\frac{\sigma_s}{r_{ij} - \sigma_{ij} + \sigma_s}\right]^{6}\right\}. \quad (1)$$

Here the molecular shape anisotropy is taken into account via an orientation-dependent core-range parameter σ_{ij} defined as

$$\frac{\sigma_{ij}}{\sigma_s} = \left\{1 - \frac{\chi}{2}\left[\frac{(\mathbf{u}_i \cdot \hat{\mathbf{r}}_{ij} + \mathbf{u}_j \cdot \hat{\mathbf{r}}_{ij})^2}{1 + \chi(\mathbf{u}_i \cdot \mathbf{u}_j)} + \frac{(\mathbf{u}_i \cdot \hat{\mathbf{r}}_{ij} - \mathbf{u}_j \cdot \hat{\mathbf{r}}_{ij})^2}{1 - \chi(\mathbf{u}_i \cdot \mathbf{u}_j)}\right]\right\}^{-1/2}, \quad (2)$$

where $\chi = (\kappa^2 - 1)/(\kappa^2 + 1)$ and $\kappa = \sigma_e/\sigma_s$, while σ_e and σ_s denote the molecular length and width, respectively. Further, the anisotropy of the attractive forces is given through the energy parameter $\varepsilon_{ij} = \varepsilon_0(\varepsilon'_{ij})^\mu(\varepsilon''_{ij})^\nu$, where ε_0 is a characteristic GB interaction energy scale, μ and ν are dimensionless parameters, and

$$\varepsilon'_{ij} = 1 - \frac{\chi'}{2}\left[\frac{(\mathbf{u}_i \cdot \hat{\mathbf{r}}_{ij} + \mathbf{u}_j \cdot \hat{\mathbf{r}}_{ij})^2}{1 + \chi'(\mathbf{u}_i \cdot \mathbf{u}_j)} + \frac{(\mathbf{u}_i \cdot \hat{\mathbf{r}}_{ij} - \mathbf{u}_j \cdot \hat{\mathbf{r}}_{ij})^2}{1 - \chi'(\mathbf{u}_i \cdot \mathbf{u}_j)}\right], \quad (3)$$

$$\varepsilon''_{ij} = [1 - \chi^2(\mathbf{u}_i \cdot \mathbf{u}_j)^2]^{-1/2}. \quad (4)$$

Here $\chi' = (\kappa'^{1/\mu} - 1)/(\kappa'^{1/\mu} + 1)$ and $\kappa' = \varepsilon_s/\varepsilon_e$, with ε_s and ε_e standing for the attractive well depths for the side-by-side and end-to-end configurations of a molecular pair, respectively. In this study we followed the Berardi et al. parametrization of the GB potential, setting $\mu = 1$, $\nu = 3$, $\sigma_e/\sigma_s = 3$, and $\varepsilon_s/\varepsilon_e = 5$[18]. For a typical rod-shaped mesogen one has $\sigma_s \approx 5 \times 10^{-10}$ m for the short molecular axis and $\varepsilon_0 = \varepsilon_s \approx 100 k_B T_{NI} = 1.38 \times 10^{-21}$ J for the characteristic energy scale. The latter estimate was made by comparing a realistic nematic-isotropic (NI) transition temperature T_{NI} in an ordinary monomeric liquid crystal (say, $T_{NI} = 355$ K) with the corresponding reduced temperature $T_{NI}^* = k_B T_{NI}/\varepsilon_0 \approx 3.55$ as obtained from Monte Carlo simulations with the original GB potential, Eq. (1)[18].

In the soft-core (SC) potential modification the strong intermolecular repulsion of the original GB interaction (1) is replaced by a significantly weaker repulsive potential. The corresponding energy contribution for the molecules i and j is assumed to increase linearly at short intermolecular distances

and is written as[16]

$$U_{ij}^{SC} = m(r_{ij} - \sigma_{ij}). \quad (5)$$

Here m regulates the slope of the potential and hence its stiffness, while σ_{ij} is the core-range parameter given by Eq. (2). Introducing a sigmoidal logistic function $f_{ij} = 1/\{1 + \exp[n(\sigma_{ij} - r_{ij})]\}$, the original GB and the SC potential can be blended continuously to yield a new combined potential

$$U_{ij}^{GBS} = (1 - f_{ij})U_{ij}^{GB} + f_{ij}U_{ij}^{SC}. \quad (6)$$

The parameter n is related to the width of the transition region where features of both potential types are present. Following Ref.[16], we set $m = -70\varepsilon_0/\sigma_s$ and $n = -100/\sigma_s$ to retain the attractive features of the original GB potential, as well as the soft repulsive core of the SC potential.

We assumed the intermolecular potential (6) to act between all mesogenic unit types in the sample, non-bonded as well as bonded. However, in order to build an elastomer, mesogens have to be linked into a network. To model main-chain polymers we introduced bonding sites at the two ends of the GB monomers[11,12]. Further, to model reticulation we placed an additional reactive site on the monomer equator, as detailed later on. Then the additional bonding energy between two bonded monomers was represented with the finitely extendable nonlinear elastic potential (FENE)[19], applied as both stretching and bending potential. In comparison with the standard Hookean spring potential the FENE potential penalises large deviations from equilibrium more severely. In addition, it also sets a maximum stretch and bend range.
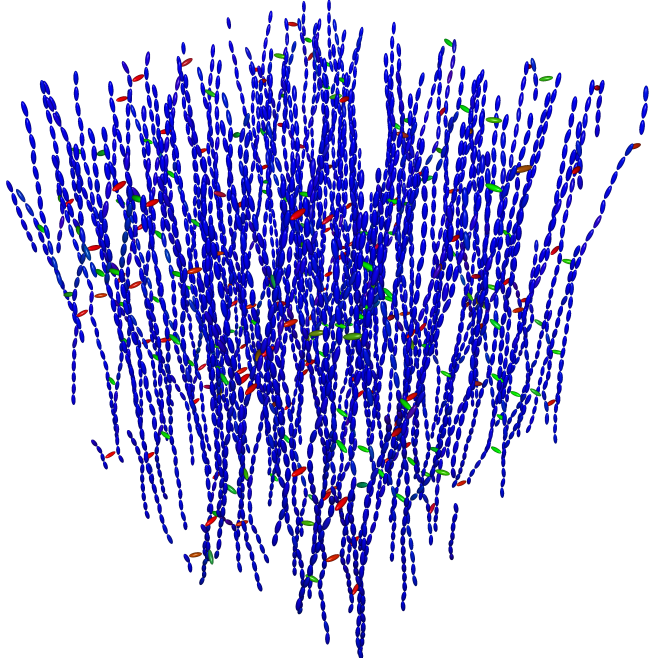
For a bond connecting two adjacent monomers i and j with instantaneous bond length s_{ij} one can calculate the deviation from its equilibrium value s_e, i. e., $\delta s_{ij} = s_{ij} - s_e$. The maximum allowed δs_{ij} is denoted by δs_m. Further, the bond angle θ_{ij} can be defined as the angle between the preferred bond directions, as imposed by each monomer[11]. Similarly, the angular deviation $\delta\theta_{ij} = \theta_{ij} - \theta_e$ from the equilibrium value θ_e is introduced for the bond angle, and the largest $\delta\theta_{ij}$ denoted by $\delta\theta_m$. Then, the FENE spring bond energy is given by[11,12]

$$U_{ij}^{FENE} = -k_s\delta s_m^2 \log\left[1 - \frac{\delta s_{ij}^2}{\delta s_m^2}\right] - k_\theta\delta\theta_m^2 \log\left[1 - \frac{\delta\theta_{ij}^2}{\delta\theta_m^2}\right]. \quad (7)$$

In Eq. (7) the first term refers to bond stretching and the second to its bending. The force constants k_s and k_θ regulate the bond stiffness for the relevant deformation mode. Here we chose $s_e = 0.15\sigma_s$, $\delta s_m = 0.25\sigma_s$, and $k_s = 500\varepsilon_0/\sigma_s^2 \approx 2.76$ N/m for stretching, and $\theta_e = 0°$, $\delta\theta_m = 150°$, and $k_\theta = 3.8 \times 10^{-4}\varepsilon_0/\text{deg}^2 \approx 1.72 \times 10^{-21}$ J/rad^2 for bending[11,12].

To obtain the total interaction energy for a system of N particles it is necessary to collect all non-bonded (soft-core GB)

Fig. 1 LCE sample network architecture as revealed after a negative pressure shock. Red, green, and blue colour correspond to molecular alignment along x, y, and z, respectively. Swelling molecules are not shown. The average polymer strand direction is parallel to the z-axis. Note the interstrand crosslinks (shown in red or green).

and bonded (FENE) intermolecular contributions. The total reduced energy (per particle) can then be written as

$$U^* = (N\varepsilon_0)^{-1} \sum_{i=1}^{N} \sum_{j=i+1}^{N} \left(U_{ij}^{GBS} + w_{ij} U_{ij}^{FENE} \right), \qquad (8)$$

where $w_{ij} = 1$ if the monomeric units i and j are bonded, and $w_{ij} = 0$ otherwise. (Only up to one bond per monomer pair is possible.) Note that the evaluation of the double sums in Eq. (8) becomes unfeasible for very large samples because of the increasing computational effort that scales as $\sim N^2$. However, since the GB-type and FENE interactions considered here are relatively short-ranged, we introduced an interaction cutoff in the calculation of U^*, together with a Verlet neighbour list for each molecule [20]. Here the selected interaction and neighbour list cutoff radii were $4\sigma_s$ and $5\sigma_s$, respectively. A further reduction of the computational cost was obtained during neighbour list calculation by using cell linked-lists [21]. In this case the resulting computational cost scales approximately linearly with N.

3 Model: Sample architecture and preparation

For simplicity, we built our elastomer sample exclusively from identical GB particles. Our intention was to produce a highly responsive main-chain LCE material suitable for actuation through temperature variation etc. Experimentally, a two-stage crosslinking procedure is needed to obtain a sample with suitable performance [22]. In the first stage polymerization proceeds to form main chain strands. The chains are then ordered by an external field (mechanical or electric), which is followed by a second polymerization leading to reticulation with a typical crosslink density below $\sim 10\%$. Hence this procedure results in an imprinted directional anisotropy, yielding a pronounced strain-alignment coupling. Imitating these experimental steps, we built our sample in an initially cubic simulation box as a regular square array of vertical polymer strands (Fig. 1). The bonding sites for molecules of each strand were located at the two molecular ends and the preferred bond direction was chosen parallel to the long axis of each molecule. In this way the vertical direction, the z-axis, became privileged, representing the direction of imprinted anisotropy. Then, each of the strands was linked via a single GB particle — acting as a crosslinker — to its nearest neighbours along x and y. The crosslink position along the z coordinate was selected at random. In this scheme the strand molecules that are additionally bonded by a crosslinker to the adjacent strand became trifunctional: the third bonding site was situated at the particle equator and the preferred bond direction was parallel to the short molecular axis. Finally, the empty space between the now connected strands was uniformly filled with non-bonded swelling GB monomers. After completing this assembly stage, the sample was uniformly compressed to remove the remaining void space.

The details for our samples are: the polymer network consists of an 11×11 square network of strands, containing 30 anisotropic beads each, plus of 2 crosslinking beads per strand. In total this amounts to 3872 GB particles building up the LCE network. Then, further 4128 GB "solvent" monomers were added to give a total of 8000 particles in the system. — For a more reliable calculation of X-ray patterns, a limited number of runs with significantly larger samples containing 216000 molecules was also carried out. These samples were obtained by maintaining the architecture and the corresponding ratios of the small samples, rescaling them by a factor of 3 along each of the Cartesian axes. — For all samples, periodic boundary conditions were applied at the simulation box boundaries.

The compression runs following each sample assembly were carried out at a reduced pressure $p^* = p\sigma_s^3/\varepsilon_0 = 10$ and resulted in a sample with reduced density $\rho^* = N\sigma_s^3/V \approx 0.287$, where V denotes the volume, approximately matching the density of the monomeric GB system considered in Ref. [18]. In the following we are going to refer to a sample obtained at
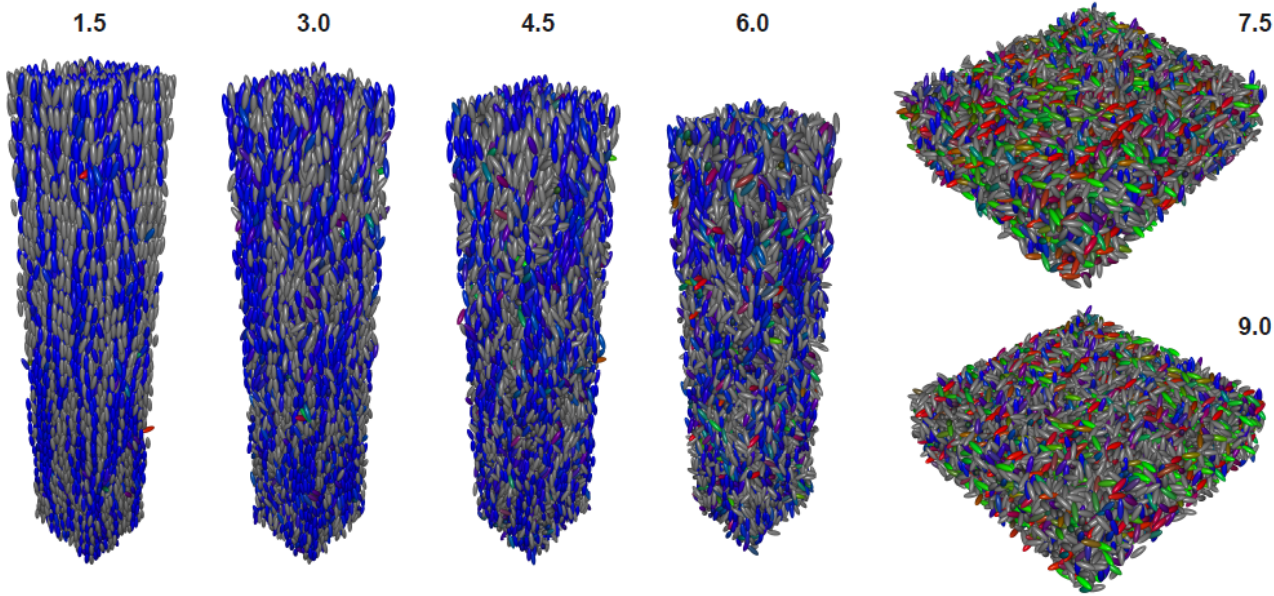
Fig. 2 Sample snapshots at different temperatures. (The corresponding T^* values are indicated above each image.) The orientation-dependent colour coding for the network particles is the same as in Fig. 1, while all non-bonded monomers are shown in grey. An elongated and ordered sample at low T^* becomes flat and disordered upon heating above the nematic-isotropic transition temperature. Smectic layering along the z-axis can be observed for $T^* = 1.5$.

this stage of the preparation procedure as to the *reference* sample.

4 Model: Monte Carlo simulations

In the studies of our main-chain LCE samples we used isobaric and isostress Metropolis-type Monte Carlo simulations[5,23] for sample preparation and for performing simulated experiments, respectively. To ensure sufficiently efficient sampling of phase space, we carried out several trial move types. (i) *Translational moves.* For this move type the selected GB particle was displaced by a randomly generated vector, maintaining particle orientation. (ii) *Rotational moves.* Here the selected particle was rotated by a random angle around a randomly selected Cartesian axis[24]. The particle centre of mass was not moved. (iii) *Bonded pair rotations.* This move type concerned only doubly linked GB particles in the polymer strands, excluding the crosslinks. The selected pair of bonded particles was rotated by a random angle about an axis connecting the far-away ends of the particle pair. (The far-away ends are bonded to the corresponding neighbours along the polymer strand.) (iv) *Resize moves.* This collective move type involved all GB particles in the sample. In the move two (out of three) sides of the simulation box were chosen at random, each of them to undergo a different random variation. The trial value for the third box side was calculated from the constant-volume con-

straint to ensure sample incompressibility. Through this move the initially cubic simulation box was deformed as a whole and gradually turned into an orthogonal parallelepiped. The polymer strands were deformed affinely, i.e., in geometric proportion to the simulation box. The trial configurations violating the maximum-length or maximum-angle constraints of the FENE potential were rejected automatically. — Note that all of the above trial move types are reversible and non-biased.

In our simulations one Monte Carlo cycle consisted of attempting translational and rotational moves for each GB particle. The sequence of particles to be rotated and moved in a MC cycle was generated by a random shuffling algorithm. In addition, bonded pair rotations were also attempted for all eligible particle pairs. Following the Metropolis algorithm[23], the proposed trial move resulting in a reduced energy change $\Delta U^* = (U^*)_{new} - (U^*)_{old}$ was accepted at temperature T with a probability $\min[1, \exp(-N\varepsilon_0\Delta U^*/k_BT)]$. — Moreover, every 5 cycles a sample resize move was attempted. In the isostress simulation, external stress was applied along the z-axis. To measure the resulting deformation, λ_z was conveniently defined as a ratio of the actual and the *reference* sample simulation box sizes along the z-axis. Further, reduced stress $\sigma^* = \Sigma_{zz}\sigma_s^3/\varepsilon_0$ was introduced, where Σ_{zz} denotes the engineering stress for stretching/compression along the z-axis, calculated with respect to the surface area corresponding to a face of the *reference* sample. A constant-

volume resize move deforming the simulation box side along z by $\Delta\lambda_z = (\lambda_z)_{new} - (\lambda_z)_{old}$ was then accepted with a probability $\min\{1, \exp\left[-N\varepsilon_0(\Delta U^* - \sigma^*\Delta\lambda_z/\rho^*)/k_BT\right]\}$ [5,25]. — Finally, for each of the trial move types the move amplitudes were adjusted on the fly during MC evolution to ensure an acceptance between 45% and 55%. At the same time it was checked by monitoring the amplitudes that these conditions were sufficient for the system to evolve. Further, the Verlet neighbour lists were refreshed after every MC cycle, while the cell-linked list updates were performed every 5000 cycles.

To provide a further simulation speedup, two different parallelization schemes were used in the MC simulation code. (i) For *small samples* ($N = 8000$), parallelization was applied only to the calculation of the interaction energies, while the Metropolis algorithm itself was not modified. Due to a rather frequent creation/annihilation of parallel threads in the simulation such a scheme does not scale well with the incresing number of threads. (ii) In *large samples* ($N = 216000$), however, in a given MC cycle the entire Metropolis procedure was distributed among parallel threads, making use of the cell linked-list structure, and taking care (with an appropriate random number generation) that the continuity of the Markov chain is not disrupted. Such a scheme requires a less frequent thread creation/annihilation and is therefore rather efficient even for a large number of parallel threads; however, it can only be implemented for a large enough sample where cell linked-lists can be established [21].

5 Observables

The most immediate observable that can be obtained from simulations is the reduced energy U^*, Eq. (8). Its fluctuations during a MC run can be related to the heat capacity of the system, C_V, whose anomalies are used in calorimetry for the detection of structural phase transitions. The corresponding dimensionless specific heat per particle can be introduced as

$$c_V^* = \frac{C_V}{Nk_B} = \frac{N(\langle U^{*2}\rangle - \langle U^*\rangle^2)}{(T^*)^2}, \qquad (9)$$

where $T^* = k_BT/\varepsilon_0$.

Another set of observables that is readily obtained from simulations are the actual sample dimensions, i.e., the simulation box sides. In our plots, the average reduced box sides λ_x, λ_y, and λ_z are displayed, where the normalization was performed with respect to the cubic *reference* sample with $\lambda_x = \lambda_y = \lambda_z = 1$.

Moreover, in liquid-crystalline systems such as LCEs it is relevant to measure or calculate nematic order parameters based on the second-rank ordering matrix. For the jth molecule with orientation $\mathbf{u}_j$ at a certain MC sample sweep this matrix reads $\mathsf{Q}_j = (1/2)(3\mathbf{u}_j \otimes \mathbf{u}_j - \mathsf{I})$, where I denotes
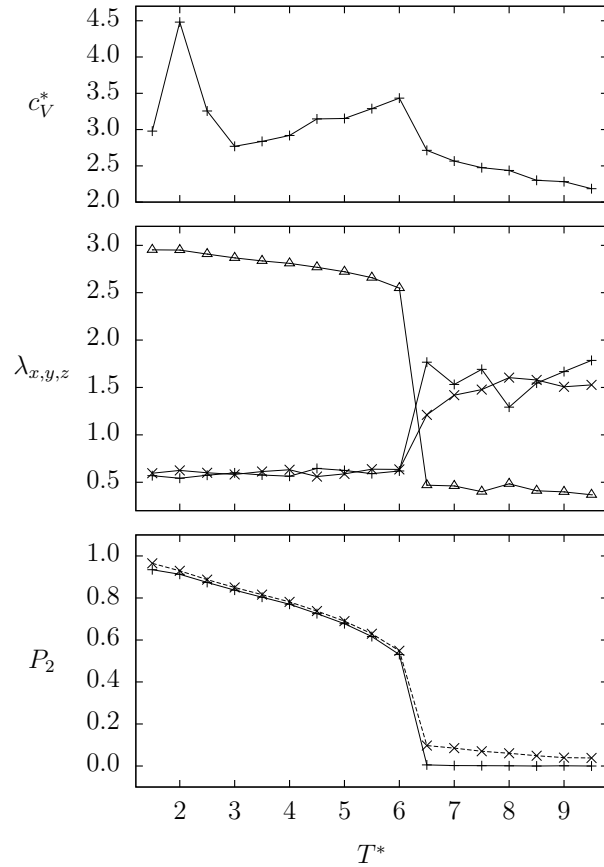
Fig. 3 Temperature scan at zero external stress. *Top.* Specific heat. *Centre.* Simulation box sides: λ_x (+), λ_y (×), and λ_z (△). *Bottom.* Nematic order parameters: global P_2 (+) and local P_2^L (×).

the identity matrix. Now one can introduce a global order parameter, P_2, obtained by calculating the largest eigenvalue of the sample-averaged ordering matrix $(1/N)\sum_{j=1}^{N} \mathsf{Q}_j$ in each MC cycle, and then subsequently averaging these eigenvalues over MC cycles. However, since LCEs show features of polymers, including possible glassy behaviour, it may also be helpful to quantify local ordering. This can be done by separately diagonalizing each of the local (molecular) ordering matrices $\langle \mathsf{Q}_j \rangle$, obtained as an average of Q_j over MC "time", providing the corresponding largest eigenvalues P_2^j for each molecule, and calculating a sample-averaged local order parameter P_2^L as $P_2^L = (1/N)\sum_{j=1}^{N} P_2^j$. Any significant deviation of P_2^L from P_2 implies a difference between ensemble and time averaging, and may be a signature of glassy ordering in the system. (Herewith P_2^L takes the role of the Edwards-Anderson order parameter introduced in spin glass systems[26].)

Experimentally, local orientational order in LCEs is often probed by deuterium nuclear magnetic resonance (^{2}H NMR)[27-30]. Quadrupolar interactions in deuterated mesogenic units result in an orientation-dependent frequency splitting[31] that, for the jth molecule, is given by $\omega_Q^j = \pm \delta\omega_Q[3(\mathbf{u}_j \cdot \mathbf{b})^2 - 1]/2$. For simplicity, here it has been assumed that the motionally-averaged electric field gradient tensor of the carbon-deuteron bond in a mesogenic molecule is effectively uniaxial and that the symmetry axis of the tensor is parallel to the long molecular axis, $\mathbf{u}_j$. Further, $\mathbf{b}$ stands for a unit vector along the NMR spectrometer magnetic field and $\delta\omega_Q$ denotes a coupling constant[31]. Note that the above averaging assumption applies well to monomeric mesogens — here the averaging merely rescales the $\delta\omega_Q$ constant, maintaining the full spectral shape — while it may be somewhat less plausible for the bonded mesogens whose motions are partially hindered. — In the present study we used our simulation output, i.e., a sequence of molecular configurations, to calculate the characteristic ^{2}H NMR spectra. Like in an actual NMR experiment, the spectra were obtained by first generating the free induction decay (FID) signal $G(t) = \langle \exp[i\int_0^t \omega_Q^j(t')\,dt']\rangle_j$, where t stands for time and $\langle \cdots \rangle_j$ denotes averaging over particles, and then Fourier-transforming it[32]. In each run, we simultaneously calculated three spectra, with the spectrometer magnetic field directed along the x, y, or z-axis. The duration of one NMR cycle, $2\pi/\delta\omega_Q$, was fixed to 1024 MC cycles, while the total length of the generated FID signal was 2^{20} MC cycles. — Translational diffusion is expected to be low in the system considered and does not significantly affect the calculated spectra.

Another important experimental technique in LCE studies, capable of probing also the positional order, is X-ray scattering. Here, in the scattered X-ray pattern calculation we employed the procedure followed by Bates and Luckhurst for a monomeric GB system[33]. The procedure as-

sumes that the scattering factor for a GB particle (represented by a uniaxial ellipsoid) is given by $\mathcal{F}_j(\mathbf{q},\mathbf{u}_j) = 3(\sin\gamma_j - \gamma_j\cos\gamma_j)/\gamma_j^3$, where $\mathbf{q}$ is the scattering vector, while γ_j carries the complete information on the particle orientation $\mathbf{u}_j$ and anisotropy[34]. Here $\gamma_j = (q\sigma_s/2)(\kappa^2\cos^2\phi_j + \sin^2\phi_j)^{1/2}$, $q = |\mathbf{q}|$, and $\cos\phi_j = (\mathbf{q}\cdot\mathbf{u}_j)/q$. ($\kappa$ and σ_s have the same meaning as in Section 2.) Then, the total scattering amplitude for a system of N ellipsoids reads $F_T(\mathbf{q}) = \sum_{j=1}^{N} \mathcal{F}_j(\mathbf{q},\mathbf{u}_j)\exp(i\mathbf{q}\cdot\mathbf{r}_j)$, where $\mathbf{r}_j$ is the position of the jth GB particle. Finally, the resulting total scattering intensity is calculated as $I(\mathbf{q}) = F_T(\mathbf{q})F_T^*(\mathbf{q})$. Note that since the scattering patterns are centrosymmetric, i.e., $I(\mathbf{q}) = I(-\mathbf{q})$, only half of each pattern needs to be actually calculated. Above we have assumed that the scattering is dominated by the mesogenic units and that the contribution originating from flexible spacers (e.g., alkyl or methylene) connecting the mesogens is negligible. This is expected to be a good approximation in view of the higher electron density in the mesogenic cores forming the elastomer chains. — The X-ray patterns were calculated every 200 MC cycles and averaged over a production period of 263×10^3 cycles. Here, rather large 216000-particle samples had to be considered in order to reduce the finite-size artifacts close to the centre of the scattered pattern.

6 Results: Temperature scans

First we performed a series of zero-stress simulations at different temperatures. All runs were launched from the reference sample and left equilibrating for at least 9×10^6 MC cycles. Then, various averages were accumulated over more than 10^6 MC cycles. Typical snapshots of the molecular organization are displayed in Fig. 2, while the temperature dependences of the specific heat, sample dimensions, and nematic order parameters are shown in Fig. 3. The specific heat anomalies in the temperature scan reveal the existence of two phase transitions. The nematic-isotropic transition, estimated to occur at $T_{NI}^* \approx 6.25 \pm 0.25$, results in a significant change both in the molecular organization as well as in sample shape. Below T_{NI}^* mesogenic units exhibit nematic ordering and the sample is elongated along the z-axis, which is consistent with the direction of the orientational anisotropy imprinted upon sample preparation. On the other hand, the sample is isotropic above T_{NI}^*, and is compressed (or flattened) along the z-axis. In both cases the sample deformation (measured from the cubic *reference* sample) is quite uniaxial.

For a monomeric soft-core GB system with the same parametrization as in Ref.[16] and density $\rho^* = 0.3$ the NI transition is seen at $T_{NI}^* \approx 4.9$. In a partially bonded system like the present one where the molecular motions are hindered due to an increased effective molecular length, the ordered system should be more stable and the NI transition is indeed observed
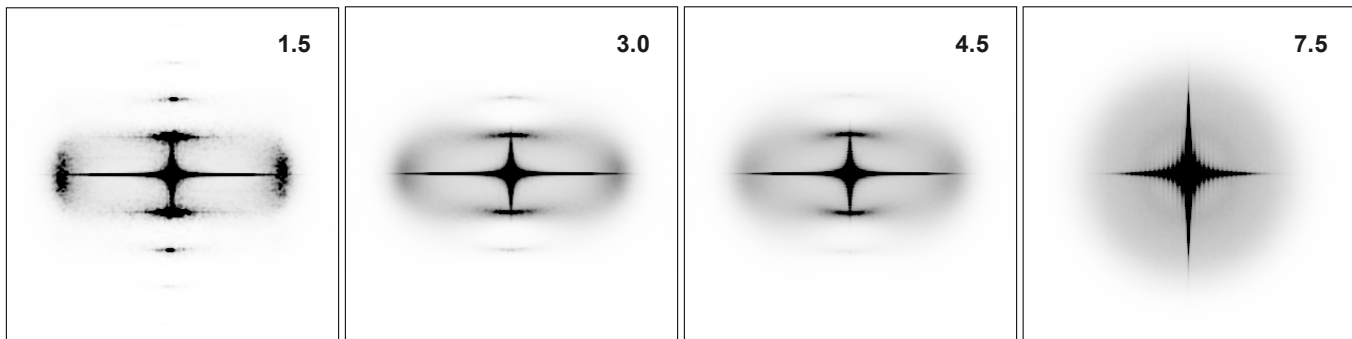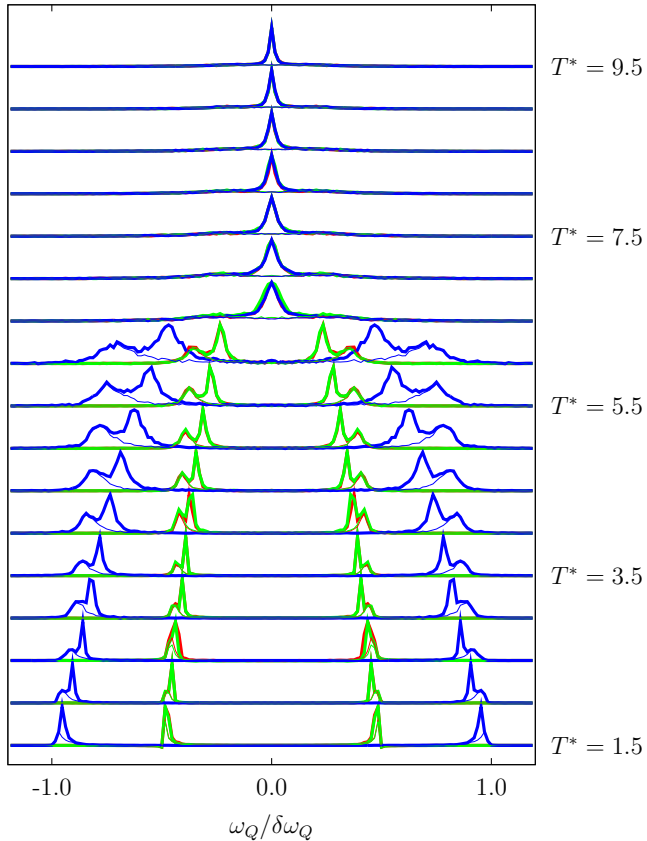
Fig. 5 Scattered X-ray patterns with indicated corresponding T^* values: Smectic ($T^* = 1.5$), nematic ($T^* = 3.0$ and 4.5), and isotropic ($T^* = 7.5$) LCE. The simulated X-ray beam was directed perpendicular to the nematic director pointing in the vertical direction. The side of each square frame in scattering vector scale corresponds to $6\pi/\sigma_s \approx 38/\text{nm}$.

at a higher temperature. Note also that at very low temperatures smectic layering occurs. The smectic-nematic (SN) transition temperature is estimated as $T^*_{SN} \approx 2.0 \pm 0.5$, which is almost the same as in the original monomeric GB system[18]. Indeed, the SN transition mainly concerns translational degrees of freedom, and the presence of the hindering intermolecular bonds is expected to play a less important role in this case.

From Fig. 3 it can be deduced that while the NI specific heat peak is well-visible but quite suppressed in comparison with the monomeric system, the NI transition in the present case is still rather sharp and discontinuous in the degree of order, P_2, as well as in sample dimensions, λ_i ($i = x, y, z$). This observation is further supported by the existence of long-lived metastable states at $T^* = 6.25$, and compares well with some (but not all) experimental studies. Namely, the NI transition observed in some early LCE samples was rather smooth due to quenched disorder or internal stresses stemming from residual irregularities, even in monodomain materials[28,35]. The importance of irregularities can, however, be reduced by decreasing crosslink concentration, or by swelling the samples with a liquid-crystalline solvent[28–30], thus driving the LCE system behaviour from supercritical (smooth) to subcritical (discontinuous). Hence, the subcriticality observed in our model sample is not really surprising: The sample is rather regular and monodomain-like by construction, and — in addition — contains a rather high percentage of monomeric liquid crystalline units. (Note that the NI transition for the pure GB monomers is discontinuous.) Recall that the only type of irreg-

ularity introduced during sample preparation is the randomness in crosslink positions, effectively resulting in moderate polymer strand length polydispersity; however, this appears not to be enough to significantly affect the overall system behaviour. We further explored this issue by running temperature scans for three more samples with different crosslink positions, keeping the crosslink concentration constant, but the results (including T^*_{NI} values) remained essentially unchanged at our present temperature resolution. For this reason the following discussion will be focused on a single LCE sample. — Note also that a single NI transition is observed despite the two-component character of the system, which suggests that there is no significant phase separation of the bonded and non-bonded (monomeric) mesogens in the temperature range examined.

Additional information can be extracted from the ^{2}H NMR spectra sequence shown in Fig. 4. In the Figure, the signal originating from the network molecules is separated for clarity from the total response that includes also the swelling monomers. First we notice that above T^*_{NI} the molecular motions (apparently fast with respect to the NMR timescale $2\pi/\delta\omega_Q$) average out the quadrupolar interactions, which results in a single spectral peak at zero splitting. Below T^*_{NI} in the nematic (and smectic) phase, however, a pronounced splitting can be observed. Note that the splitting for $\mathbf{b}\|\mathbf{z}$ is roughly twice the value obtained for $\mathbf{b} \perp \mathbf{z}$. (Here $\mathbf{z}$ denotes a unit vector along the z-axis.) Further note that each of the spectral peaks has a pronounced structure: The contribution from
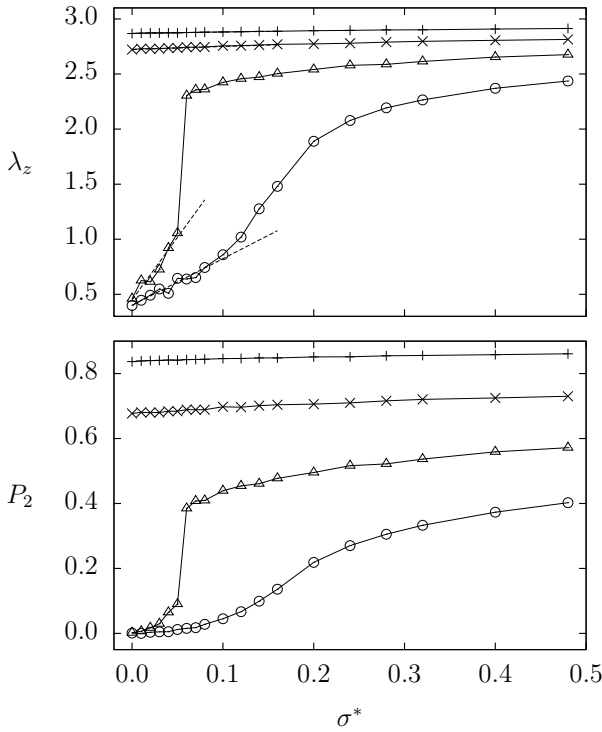
the bonded network is located at a somewhat higher splitting value than that of the monomers. This differentiation may be attributed to a lower degree of order for the non-bonded monomer molecules in comparison with the bonded network ones. For example, assuming the spatial variation of the local nematic director to be negligible, from the spectra simulated at $T^* = 3.0$ one can estimate the corresponding approximate P_2 values as 0.88 ± 0.02 and 0.82 ± 0.02 for the network and monomer GB particles, respectively. Despite the even larger difference in the degree of order of the two subsystems observed at $T^* = 6.0$, i.e., slightly below the NI transition, there seems to be a single NI phase transition, as already stated above. However, there also seems to be some residual paranematic order above T_{NI}^* due to the bonded network, which reflects in nonzero values of the local P_2^L order parameter for $T^* > T_{NI}^*$ (Fig. 3, *bottom*). In the spectra, this paranematic order results in some barely visible signal outside the peak centered at $\omega_Q = 0$.

Lowering the temperature brings about an increased NMR splitting as the order increases (Fig. 4), but NMR does not show the onset of smectic order or unveil the nature of the low-temperature phase transition seen by calorimetry. On the other hand, scattered X-ray patterns can be particularly useful in assigning the nature of the low-temperature phase; therefore, some of the calculated patterns are presented in Fig. 5. Starting with the high-temperature pattern for $T^* = 7.5$, one can notice a circular halo instead of a diffuse ring expected from lateral short-range intermolecular correlations in an isotropic liquid crystal. The unexpected absence of a pronounced diffuse ring may be partly attributed to the soft-core potential allowing for non-negligible particle overlap at high temperatures, which can be confirmed also by inspecting the corresponding pair correlation functions. Cooling the sample to $T^* = 4.5$, the scattered pattern becomes nematic-like, with very diffuse lateral arcs and two marked reflections along the vertical axis corresponding to the orientation of the nematic director. Note that here and at lower T^* the particle overlap becomes almost negligible. At $T^* = 3.0$, still in the nematic phase, the pattern is similar to the previous one, with the diffuse lateral arcs slightly more pronounced. Finally, for $T^* = 1.5$ the two lateral arcs become much narrower, which corresponds to increased orientational order, while a second order of diffraction along the director and a significant increase in intensity of the first-order peaks indicate the onset of a smectic-like layering. The first-order peaks can be observed at $q_\parallel \approx (0.33 \pm 0.01) \times 2\pi/\sigma_s$ from the centre, while the lateral arcs peak at $q_\perp \approx (0.99 \pm 0.01) \times 2\pi/\sigma_s$. Both results are compatible with rather closely packed layered GB particles $3\sigma_s$ long and σ_s wide, as used in our simulations. Note also that the central cross-like structure in all patterns is a finite-size artifact and should be ignored[33].

Fig. 4 ^{2}H NMR spectra: A temperature scan with the spectrometer magnetic field **b** applied along x, y, and z-axis shown in red, green, and blue, respectively. The contribution originating from the elastomeric network (light lines) is shown separately from the total NMR signal (heavy lines) that includes the swelling monomers as well. The overlap of the **b**||**x** and **b**||**y** spectral sets implies uniaxial molecular ordering with the respect to the z-axis.

7 Results: Stress-strain runs

In a LCE material, orientational ordering can be induced not only by decreasing temperature, but also by applying a mechanical field, i.e., external stress. Here stress was applied to equilibrated samples at $T^* = 3.0$ and $T^* = 5.0$ in the nematic phase, as well as to samples at $T^* = 7.0$ and $T^* = 9.0$ in the isotropic. For every value of reduced stress σ^*, at least 4×10^6 MC cycles were performed for further equilibration and at least 10^6 for production. In all cases stress was applied along the z-axis, i.e., parallel to the nematic director, if existent. (The case where the stress is applied perpendicular to the nematic director is expected to invoke soft elastic deformation modes and will not be considered here.)

The stress-strain isotherms are displayed in Fig. 6. Pulling along the z-axis from the nematic phase, the degree of order is enhanced and the sample slightly elongated. The corresponding elastic moduli are estimated to be 770 MPa and 310 MPa for $T^* = 3.0$ and $T^* = 5.0$, respectively, which exceeds the experimental values by more than one order of magnitude [37,38]. Recall, however, that in both cases the polymer strands are highly ordered already prior to the application of stress, especially for the lower temperature, and that hence the additional elongation mainly comes from extending the FENE bonds. This and the resulting decrease of the elastic modulus with increasing temperature suggest that the observed elasticity is energetic rather than entropic. This is in agreement with the absence of hairpins in our samples that could give rise to entropic rubber elasticity in a highly aligned sample [39,40]. (Note that the average distance between crosslinks along a polymer strand is only 7.5 GB units.)

In the isotropic phase, the pulling starts from a disordered sample. For $T^* = 7.0$, there is a discontinuous stress-induced isotropic-to-nematic transition at $\sigma^* \approx 0.05$. For $T^* = 9.0$, on the other hand, there is no discontinuity in the stress-strain curve. Consequently, there seems to be a critical point in between the two isotherms. Note that such critical behaviour is consistent with theoretical predictions based on symmetry arguments [36] and with the predictions of an early lattice model for LCE [5]. — Again, one can estimate the elastic moduli for small deformations and low σ^*; the results for $T^* = 7.0$ and $T^* = 9.0$ are 210 kPa and 410 kPa, respectively, and compare reasonably well with experiment [38]. Thus, in comparison with the nematic phase, our LCE material is substantially softer when it is isotropic. And, even more importantly, now there is an increase in the elastic modulus with increasing temperature, which may be a signature of entropic elasticity. This phenomenon occurs only if the polymer strands are capable of sampling different pathways between the crosslinks; in our samples this indeed is possible to some extent (see, e.g.,the calculated ^{2}H NMR spectra) in the disordered isotropic phase, but not in the highly ordered nematic or smectic ones.

Fig. 6 Stress-strain isotherms: Sample dimension along the z-axis (*top*) and the global nematic order parameter (*bottom*); $T^* = 3.0$ (+), $T^* = 5.0$ (×), $T^* = 7.0$ (△), and $T^* = 9.0$ (○). Here $\sigma^* = 0.1$ approximately corresponds to 1.1 MPa engineering stress. The dotted lines represent the linear fits used to estimate the elastic moduli.

8 Conclusions

We have performed a series of large-scale Monte Carlo simulations of swollen main-chain liquid crystal elastomers. The simulations were based on an off-lattice model consisting of monomer chains made of soft Gay-Berne ellipsoidal anisotropic beads, connected by FENE springs and reticulated in the aligned state with a small number ($\sim 6\%$) of short connecting GB linkers. In addition, the samples were swollen with a significant amount of GB monomers.

The properties of this simple softly repulsive-attractive network reproduce the key features of swollen main-chain elastomers, e.g., a pronounced strain-alignment coupling and the existence of nematic-isotropic and smectic-nematic order-disorder phase transitions. In our model system, the isotropic-nematic transition is a well-defined first-order transition and takes place at a higher temperature than in the corresponding monomeric system. It is accompanied by notable sample deformation and a significant change in the simulated ^{2}H NMR spectra. Moreover, the nematic-smectic transition results in a layered system and thus reflects in the predicted X-ray scattering patterns. Both transitions are also visible in the simulated calorimetric data.

Moreover, we have performed virtual stress-strain experiments, both in the nematic and in the isotropic phase, with the external stress applied along the director in the former case. The elastic response in the isotropic phase shows features of entropic rubber elasticity, with a rather low elastic modulus, comparable to that measured in real samples. On the contrary, in the highly ordered nematic the material turns out to be rather stiff. All in all, the obtained stress-strain isotherms agree well with the critical behaviour predicted by an earlier lattice model, as well as with the behaviour of real weakly crosslinked and/or swollen LCE materials.

9 Acknowledgement

References

1 M. Warner and E. M. Terentjev, *Liquid Crystal Elastomers*, Oxford University Press, Oxford, 2003.

2 D. J. Broer, G. P. Crawford, and S. Žumer, *Cross-Linked Liquid Crystalline Systems. From Rigid Polymer Networks to Elastomers*, CRC Press, Boca Raton, 2011.

3 C. Ohm, M. Brehmer, and R. Zentel, *Adv. Mater.*, 2010, **22**, 3366.

4 J. V. Selinger and B. R. Ratna, *Phys. Rev. E*, 2004, **70**, 041707.

5 P. Pasini, G. Skačej, and C. Zannoni, *Chem. Phys. Lett.*, 2005, **413**, 463.

6 G. Skačej and C. Zannoni, *Eur. Phys. J. E*, 2006, **20**, 289.

7 G. Skačej and C. Zannoni, *Eur. Phys. J. E*, 2008, **25**, 181.

8 D. Kramer and H. Finkelmann, *Soft Matter*, 2011, **7**, 1861.

9 M. Warner, in D. J. Broer, G. P. Crawford, and S. Žumer, *Cross-Linked Liquid Crystalline Systems. From Rigid Polymer Networks to Elastomers*, CRC Press, Boca Raton, 2011, p. 487.

10 A. V. Lyulin, N. K. Balabaev, and M. Michels, *Macromolecules*, 2003, **36**, 8574.

11 R. Berardi, D. Micheletti, L. Muccioli, M. Ricci, and C. Zannoni, *J. Chem. Phys.*, 2004, **121**, 9123.

12 D. Micheletti, L. Muccioli, R. Berardi, M. Ricci, and C. Zannoni, *J. Chem. Phys.*, 2005, **123**, 224705.

13 D. Micheletti, *Modelling and simulation of liquid-crystal polymers*, Ph. D. Thesis, University of Bologna (2006).

14 K. Urayama, S. Honda, and T. Takigawa, *Macromolecules* 2005, **38**, 3574.

15 K. Urayama and T. Takigawa, in D. J. Broer, G. P. Crawford, and S. Žumer, *Cross-Linked Liquid Crystalline Systems. From Rigid Polymer Networks to Elastomers*, CRC Press, Boca Raton, 2011, p. 473.

16 R. Berardi, C. Zannoni, J. Lintuvuori, and M. Wilson, *J. Chem. Phys.*, 2009, **131**, 174107.

17 J. G. Gay and B. J. Berne, *J. Chem. Phys.*, 1981, **74**, 3316.

18 R. Berardi, A. P. J. Emerson, and C. Zannoni, *J. Chem. Soc. Faraday Trans.*, 1993, **89**, 4069.

19 R. B. Bird, R. C. Armstrong, and D. Hassager, *Dynamics of Polymeric Liquids*, J. Wiley, New York, 1971.

20 L. Verlet, *Phys. Rev.*, 1967, **159**, 98.

21 M. P. Allen and D. J. Tildesley, *Computer Simulations of Liquids*, Clarendon Press, Oxford, 2000.

22 J. Küpfer and H. Finkelmann, *Macromol. Chem. Rapid Commun.*, 1991, **12**, 717.

23 D. Frenkel and B. Smit, *Understanding Molecular Simulation: From Algorithms to Applications*, Academic Press, San Diego, 2002.

24 J. A. Barker and R. O. Watts, *Chem. Phys. Lett.*, 1969, **3**, 144.

25 G. Raos and G. Allegra, *J. Chem. Phys.*, 2000, **113**, 7554.

26 S. F. Edwards and P. W. Anderson, *J. Phys. F: Met. Phys.*, 1975, **5**, 965.

27 S. Disch, C. Schmidt, and H. Finkelmann, *Macromol. Rapid Commun.*, 1994, **15**, 303.

28 A. Lebar, Z. Kutnjak, S. Žumer, H. Finkelmann, A. Sánchez-Ferrer, and B. Zalar, *Phys. Rev. Lett.*, 2005, **94**, 197801.

29 G. Cordoyiannis, A. Lebar, B. Zalar, S. Žumer, H. Finkelmann, and Z. Kutnjak, *Phys. Rev. Lett.*, 2007, **99**, 197801.

30 G. Cordoyiannis, A. Lebar, B. Rožič, B. Zalar, Z. Kutnjak, S. Žumer, F. Brömmel, S. Krause, and H. Finkelmann, *Macromolecules*, 2009, **42**, 2069.

31 R. Y. Dong, *Nuclear Magnetic Resonance of Liquid Crystals*, Springer Verlag, New York, 1994.

32 C. Chiccoli, P. Pasini, G. Skačej, S. Žumer, and C. Zannoni, *Phys. Rev. E*, 1999, **60**, 4219.

33 M. A. Bates and G. R. Luckhurst, *J. Chem. Phys.*, 2003, **118**, 6605.

34 A. Guinier and G. Fournet, *Small Angle Scattering of X-rays*, Wiley, New York, 1955.

35 J. V. Selinger, H. G. Jeon, and B. R. Ratna, *Phys. Rev. Lett.*, 2002, **89**, 225701.

36 P.-G. de Gennes, *C. R. Acad. Sc. Paris*, 1975, **281**, 101.

37 E. Nishikawa, H. Finkelmann, and H. R. Brand, *Macromol. Rapid Commun.*, 1997, **18**, 65.

38 P. Beyer, E. M. Terentjev, and R. Zentel, *Macromol. Rapid Commun.*, 2007, **28**, 1485.

39 J. M. Adams and M. Warner, *Eur. Phys. J. E*, 2005, **16**, 97.

40 M. Tokita, H. Tagawa, H. Niwano, K. Osada, and J. Watanabe, *Jpn. J. Appl. Phys.*, 2006, **45**, 1729.